Sensors & Diagnostics

PAPER

View Article Online
View Journal | View Issue

Cite this: *Sens. Diagn.*, 2024, **3**, 698

Self-powered triboelectric nanogenerator with enhanced surface charge density for dynamic multidirectional pressure sensing†

Jiaqi Wu, [ab] Yu Zhang[c] and Xin Ting Zheng *[a]

In the rapidly evolving landscape of the internet of things (IoT) and the burgeoning field of biomedical applications, development in human–machine interfaces and human motion monitoring has accentuated the need for real-time pressure sensing. However, the challenge of developing a sensor that combines high sensitivity in the low pressure range with real-time remote sensing capability has remained a significant obstacle in both fields. Herein, a self-powered triboelectric nanogenerator (TENG) based pressure sensor (STEPs) with real-time remote sensing ability is proposed to meet these critical demands, offering high sensitivity in the range of 0–70 mmHg, catering to the needs of human–machine interface and biomedical applications. The STEPs introduces an innovative composite material, blending polydimethylsiloxane (PDMS), carbon black (CB), and polyvinylpyrrolidone (PVP) for improved sensing performance, then this is subjected to ultrasonication and degassing to ensure homogeneous dispersion. The doping of CB and PVP at optimal percentages into the PDMS matrix of the STEPs, together with a unique three-dimensional structure of the sensor, achieves an optimized surface charge density, leading to a high sensitivity 2.61 ± 0.02 mV mmHg^{-1}, as compared with previous works. A wireless measurement and data transfer system, established between a STEPs array for multidirectional pressure sensing and a remote readout device following the Transmission Control Protocol (TCP), further enables real-time remote display of pressure readings. This research underscores the novelty and broad applicability of this sensor, with the potential to revolutionize self-powered wearable sensors in both human–machine interface and biomedical applications.

Received 17th January 2024,
Accepted 2nd March 2024

DOI: 10.1039/d4sd00019f

rsc.li/sensors

1. Introduction

Technological advancements in virtual reality (VR) and human–machine interfaces (HMIs) are redefining interactive technology, offering immersive experiences and enhanced human–device interactions.[5–10] At the core of these advancements lies the sophisticated integration of pressure sensing technologies, crucial for crafting interactive environments that mimic real-world dynamics, facilitating nuanced user input to translate them into more precise and responsive control systems, and providing essential data for real-time decision-making and patient monitoring.[5,11] However, precise control and response systems in applications including HMIs rely on accurate detection of mechanical signals, fast response, *etc.* In the field of pressure sensing, significant advancements have been achieved through novel material integrations and inventive design methodologies. Various types (piezoresistive, capacitive, piezoelectric, triboelectric) of pressure sensors have been explored, each with distinct mechanisms and landmark achievements including enhanced sensitivity, miniaturization potential and a wide range of applications.[12–14]

Among the sensing principles, the triboelectric nanogenerator (TENG) is a promising candidate due to it offering an unparalleled blend of efficiency, low cost and versatility, making it ideal for sensitive and real-time pressure measurement applications.[15–23] The TENG stands out when comparing other principles (piezoresistive, capacitive, piezoelectric) for its swift response to dynamic high-frequency application of mechanical force and pressure, and the ability to detect both approaching and contacted forces. The TENG principle, based on converting mechanical energy into electrical energy through contact electrification and electrostatic induction, enables the creation of responsive sensors that operate independently without using external power sources, a critical attribute for portable and wearable technologies. Recent developments in the field focusing on enhancing the output of TENGs include selection and

[a] *Institute of Materials Research and Engineering (IMRE), Agency for Science, Technology and Research (A*STAR), 2 Fusionopolis Way, Innovis #08-03, Singapore 138634, Republic of Singapore. E-mail: zhengxt@imre.a-star.edu.sg*
[b] *NUS High School of Mathematics and Science, 20 Clementi Avenue 1, Singapore 129957, Republic of Singapore*
[c] *Department of Electrical and Computer Engineering, National University of Singapore, 4 Engineering Drive 3, Singapore 117583, Republic of Singapore*
† Electronic supplementary information (ESI) available. See DOI: https://doi.org/10.1039/d4sd00019f

optimization of materials, modification of chemical compositions, and innovative design of surface structures and device architecture.[24–32] Nevertheless, these achievements are limited by complex fabrication processes and challenges in scaling. Moreover, there is little focus on low-pressure scenarios of 0–70 mmHg, which is the range required for various human–machine interface and biomedical applications such as tourniquets, compression therapy, intermittent pneumatic compression, and orthopaedic bracing.[33–39] Consequently, designing the optimal sensor morphology and selecting suitable materials for TENGs in the low pressure range using a simple, cost-effective, and scalable method is still a significant challenge, especially when effectively balancing sensitivity, accuracy, and real-time remote sensing capabilities.

In addressing the identified challenges, our research has led to the development of an innovative self-powered TENG pressure sensor (STEPs). The STEPs operates on single electrode mode of TENG, featuring flexible polydimethylsiloxane (PDMS) cylinders as a supporting structure and a unique sensing structure, which was evaluated between two different configurations: cuboid, and cone. The sensitivity was further optimized by the strategic doping of carbon black (CB) and polyvinylpyrrolidone (PVP) into the PDMS matrix to obtain the optimal content ratio for the highest achievable charge trapping ability to enhance open-circuit voltage (V_{oc}) response. Moreover, the STEPs array allows for precise determination of the location and V_{oc} of each sensor, thereby enabling accurate assessment of the direction and magnitude of the applied pressure. In applications encompassing human motion monitoring and various biomedical domains, a wireless system is imperative to collate and transmit data to remote devices, including mobile phones, as the pressure sensors are strategically placed across different body regions or discreetly embedded beneath bandages. We have thereby integrated the STEPs with a wireless data transmission system, which facilitates real-time remote pressure monitoring. These features underscore the sensor's potential for application in self-powered wearable devices, due to its simple fabrication process and highly sensitive wireless dynamic multidirectional pressure sensing abilities at low pressure scenarios. The STEPs presents an advancement in pressure sensing technology, showing potential for further development in biomedical and interface applications.

2. Experimental section

2.1. Chemicals, materials, and equipment

Sylgard 184 Silicon Elastomer kit, containing pure PDMS base and a silicon elastomer curing agent, was purchased from Dow Corning Corporation. CB was purchased from Cabot Corporation. PVP K90 was purchased from Wako Pure Chemical Industries, Ltd. The thermal Barnstead vacuum and thermal control unit were both purchased from Thermo Fisher Scientific Pte Ltd and used for the degassing and curing process of PDMS, respectively. The Bransonic ultrasonic bath was purchased from Branson Ultrasonics Corporation for ultrasonication processes. The Kikuhime pressure sensor (small) was purchased from ZiboCare Denmark and was used to measure pressure applied to the STEPs. The μStat 8000 Multi potentiostat/galvanostat was purchased from Metrohm and was used to detect the corresponding V_{oc} of the STEPs under different pressures.

2.2. Fabrication of STEPs and measurement

The STEPs mold was designed in CAD software (Fusion360, US) and printed with a stereolithography 3D printer (Form 3B+, US). To prevent PDMS adhesion to the 3D printed mould, it was baked at 65 °C for 6 hours and subsequently salinized by vapour deposition of 1*H*,1*H*,2*H*,2*H*-perfluorooctyl-trichlorosilane for 1 hour.

The synthesis process of the STEPs is delineated in Fig. 1a. Initially, a homogenous mixture was prepared by blending PDMS with different weight percentages of CB (0, 2, 4, 6, and 8 wt%) and PVP K90 (0, 2, 4, 6, and 8 wt%). To ensure a uniform dispersion of CB and PVP within the PDMS matrix, the mixture was subjected to mechanical stirring, followed by ultrasonication and degassing, each for 1 hour. Subsequently, Sylgard 184 silicone elastomer curing agent was incorporated into the CB/PVP/PDMS blend at a ratio of 1 : 10 relative to the PDMS base. After thorough mixing, the resultant mixture was cast into molds featuring conical or cuboid recesses. This was followed by a degassing and ultrasonicating step for 1 hour each and a curing phase at 80 °C for 2 hours. Upon curing, the sensing structure was enveloped with a PDMS prepolymer, which was formulated at a ratio of 10 : 1 for the polymer base to the curing agent. This prepolymer served to occupy the empty cavities within the mold, thus establishing a structural scaffold for the sensor. A subsequent degassing step was performed before subjecting to a second thermal curing at 80 °C for an additional 2 hours, culminating in the formation of an integrated sensor-support architecture. The whole structure was demolded together. To complete the fabrication, a copper electrode was affixed atop the structure, and the support cylinders were interfaced with another discrete copper electrode.

We engineered a series of CB/PVP/PDMS composites by varying the weight percentages of CB and PVP within the PDMS matrix. To facilitate a clear and concise nomenclature within this study, the composites are denoted as "C_xP_y", where '*x*' and '*y*' represent the weight percentages of CB and PVP, respectively, incorporated into PDMS. For instance, the designation C_2 corresponds to a composite containing 2 wt% CB, while C_2P_4 represents a composite with 2 wt% CB and 4 wt% PVP. A systematic investigation was conducted on composites with variations including varying weight percentages of CB and PVP, as well as dual-doped systems such as C_2P_2, C_2P_4, C_2P_6, C_2P_8, and C_2P_{10}. Each formulation was meticulously prepared and studied to elucidate the influence of CB and PVP concentrations on the physicochemical properties of the resultant composites. Informed consent was obtained from the volunteer (XTZ) prior to the participation in the motion detection demonstration.

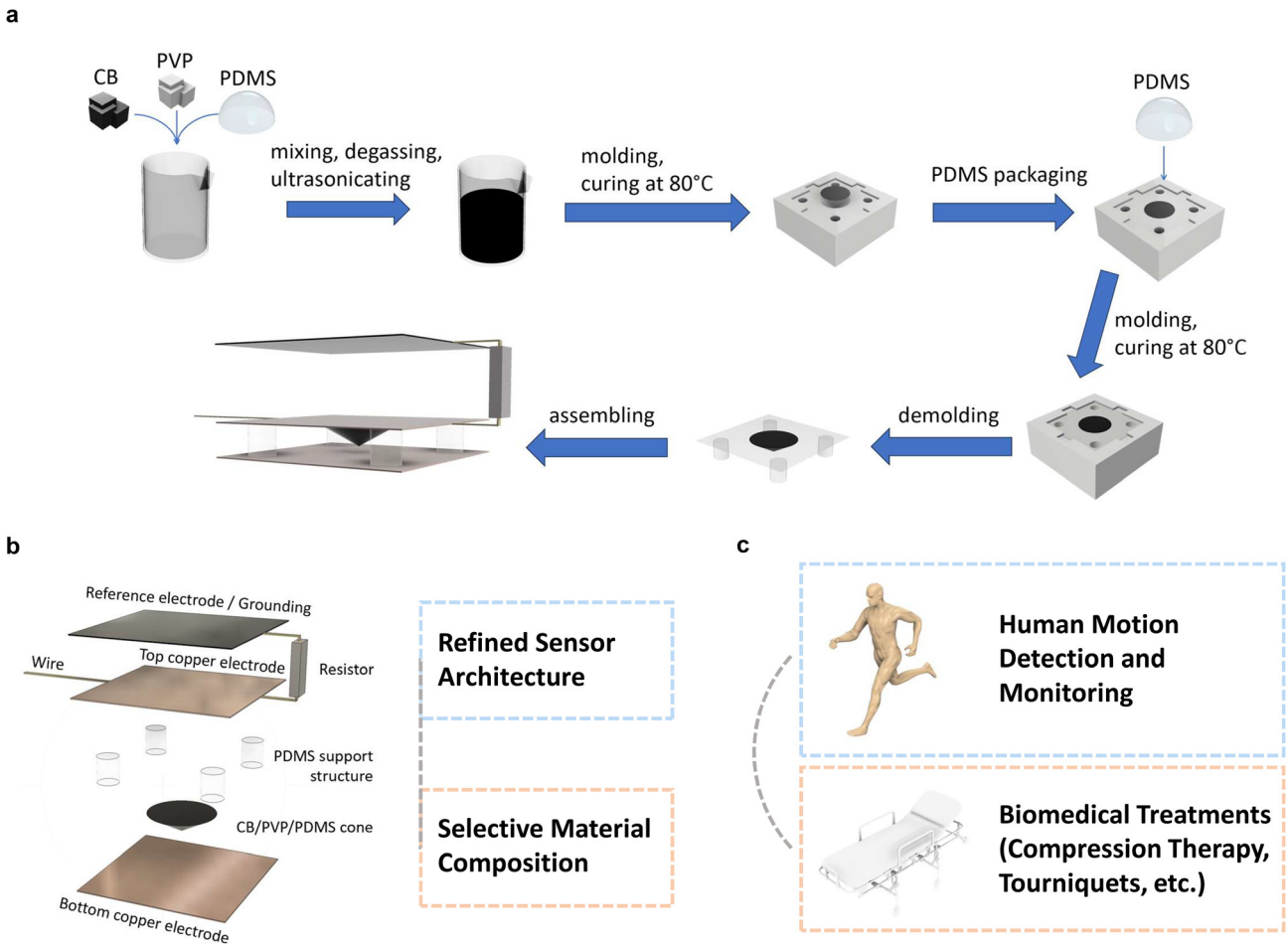

Fig. 1 Overview of the STEPs. (a) Schematic diagram of the fabrication process of the STEPs based on CB/PVP/PDMS composites. (b) Exploded view of the STEPs with cone structure. (c) Biomedical applications of the STEPs.

2.3. Statistical analysis

Error bars represent mean ± standard deviation (SD) which were calculated using Origin software. Linear fitting of calibration plots and statistical tests were also performed using Origin software. A two-sample *t*-test was performed: n. s. = not significant; $*p < 0.05$, $**p < 0.01$, $***p < 0.001$.

2.4. Simulation

Deformation of the cone-shaped or cuboid-shaped CB/PVP/PDMS structure will enhance its electron accepting ability, which is a key factor affecting charge transfer during contact electrification and thereby the performance of the STEPs. The choice of the Mooney–Rivlin material model is critical for accurately representing the hyperelastic behaviour of these materials. This model facilitates the calculation of von Mises stress, crucial for assessing material yield or failure under complex loading conditions. The Mooney–Rivlin constitutive model describes the strain energy density function (W_s) using two invariants of the Cauchy–Green deformation tensor, denoted as $\boldsymbol{I}_1$ and $\boldsymbol{I}_2$:

$$W_s = C_{10}(\boldsymbol{I}_1 - 3) + C_{01}(\boldsymbol{I}_2 - 3) + 0.5k(J_{el} - 1)^2 \quad (1)$$

Here, $\boldsymbol{I}_1$ and $\boldsymbol{I}_2$ are the first and second invariants of the deformation tensor, respectively, which encapsulate the material's deformation without reference to the coordinate system. The term $\boldsymbol{I}_1 - 3$ represents the deviatoric (distortional) strain energy associated with changes in the shape of the material, while $\boldsymbol{I}_2 - 3$ is included to account for the additional material response under complex loading conditions. The constants $C_{10} \approx 0.27$ MPa and $C_{01} \approx 0.0108$ MPa are material parameters that dictate the stress–strain relationship in the linear and non-linear regions, respectively.[40] The $0.5k(J_{el} - 1)^2$ term represents the volumetric strain energy, where k is the bulk modulus indicating resistance to volumetric deformation, and J_{el} is the elastic volume ratio. The quadratic form is chosen over other potential models (*e.g.*, linear) because it provides a more realistic representation of the material's response under compression, ensuring that the pressure remains bounded as the volume approaches the incompressible limit.[41]

In this framework, the equilibrium of forces within PDMS under applied pressure is described by:

$$0 = \nabla\cdot(\boldsymbol{F}\boldsymbol{S}^{T}) \quad (2)$$

This equation states that the divergence of the product of the deformation gradient tensor ($\boldsymbol{F}$) and the transpose of the second Piola–Kirchhoff stress tensor ($\boldsymbol{S}$) is zero, signifying mechanical equilibrium.[42] In this model, $\boldsymbol{F}$ captures the local deformation of the material, while $\boldsymbol{S}$ represents the internal stress state of the material which is related to the strain energy density function (W_s).

The detailed setup in COMSOL Multiphysics is shown in Fig. S1 and S2.† By employing the Mooney–Rivlin model, the von Mises stress of the CB/PVP/PDMS layer within the STEPs can be simulated with high accuracy. This modelling approach allows for precise prediction of deforming under various pressures applied, which is essential for explaining the difference in performance for differing sensor morphology.

3. Results and discussion

3.1. Working principle of the STEPs

Fig. 1b illustrates the exploded view of the STEPs with cone structure. It is developed with refined sensor morphology and selective material composition to achieve better performance. Due to its small size and light weight (0.88 g), it shows great potential in wearable sensor applications, including human motion monitoring and biomedical treatments (Fig. 1c).

TENGs operate based on the coupling of triboelectrification and electrostatic induction. When two different materials come into contact, due to triboelectrification, surface charge transfer occurs at the contact area and electrons are transferred from one material to the other, resulting in opposite charges on two opposing surfaces.[15] In our STEPs, the triboelectric layers are engineered from a CB/PVP doped PDMS matrix, working in conjunction with a copper (Cu) electrode. The schematic diagram of the working principle of the STEPs is demonstrated when pressure is applied, as shown in Fig. 2a. The original state of the STEPs just after assembly is shown in Fig. 2a-i. Upon the application of pressure (Fig. 2a-ii), the conical structure within the sensor comes into contact with the Cu electrode and partially deforms. This interaction, governed by the triboelectrification effect and the pronounced electronegativity of the CB/PVP/PDMS composites, results in the induction of negative charges on the composite surface, while the Cu electrode acquires triboelectric charges of opposite polarity. The subsequent separation of the cones from the Cu surface, driven by the release of the applied pressure, prompts the flow of electrons through the external circuit to neutralize the potential difference created by the charge induction (Fig. 2a-iii). Once the external pressure is fully withdrawn, the system re-establishes an equilibrium between the positive and negative charges. As the cycle continues with the cones re-approaching the Cu electrode, electrons are drawn back through the circuit (Fig. 2a-iv). This cyclical process of

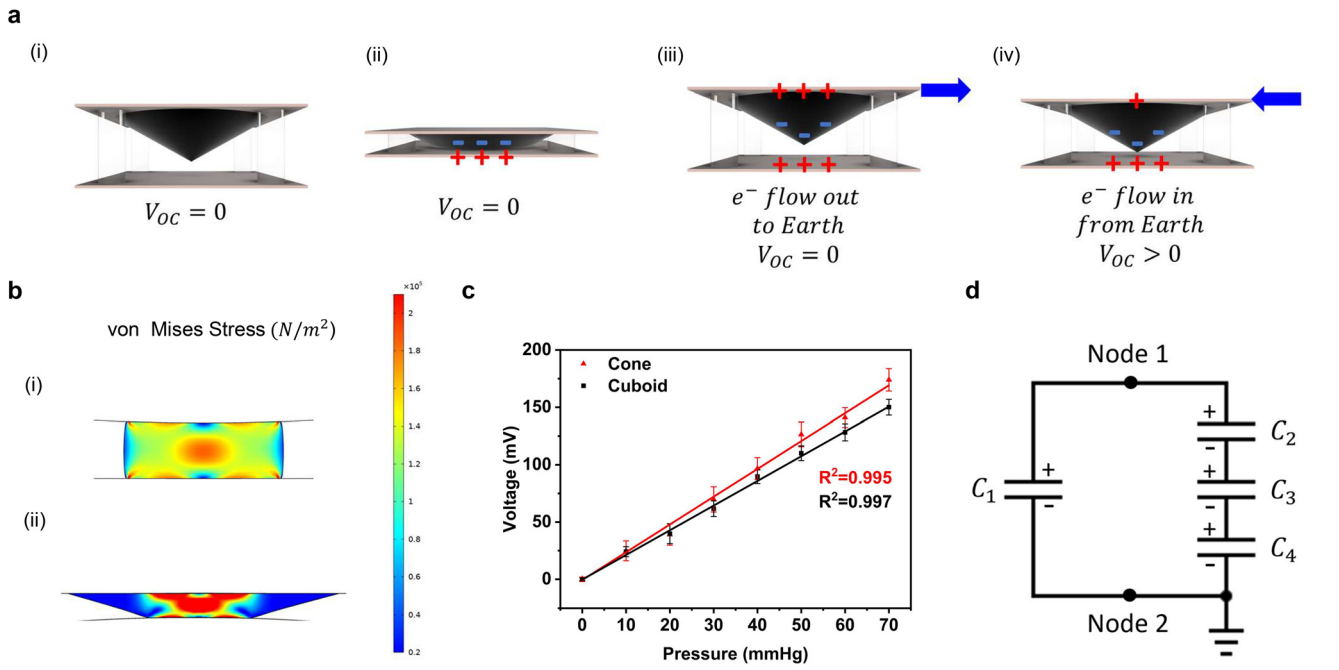

Fig. 2 Mechanical and electrical properties of the STEPs. (a) Schematics of the sensing principle under applied pressure. (i) Original state, (ii) under high pressure, (ii) release of pressure, and (iv) next pressure application. (b) Simulation results showing von Mises stress during triboelectrification within (i) cuboid structure and (ii) cone structure. (c) V_{oc} responses and sensitivity of the STEPs under pressure ranging from 0 to 70 mmHg for the C_2 cone-shaped sensor and cuboid-shaped sensor (n = 5). (d) Corresponding equivalent circuit of the STEPs under open-circuit conditions.

compression and relaxation, leading to the repeated approach and divergence of the triboelectric layers, induces a changing V_{oc} between electrodes, which is the fundamental electrical output of the STEPs.[15]

3.2. Geometric optimization of the STEPs

The geometric configuration of a TENG profoundly impacts its efficacy, particularly concerning energy conversion efficiency and the dynamics of the V_{oc} due to varying deformation capability. In this study, we investigated the influence of structural shape on the performance of TENGs by employing cone-shaped and cuboid-shaped STEPs while maintaining identical heights for both configurations and consistent volume. CB at 2 wt% is used for this experiment. Theoretically, according to the simulation shown in Fig. 2b and Video S1,† during triboelectrification, the von Mises stress of the cone culminates at the apex, representing a more pronounced mechanical deformation that increases the negative triboelectric property of CB/PDMS structure. This increases the charge transfer between materials, thereby improving the output performance of the TENG.[15,43,44] Therefore, the cone-shaped STEPs should have higher sensitivity than the cuboid-shaped STEPs. Empirical data corroborate these theoretical predictions, as delineated in Fig. 2c, which illustrates the comparative voltage outputs during press–release cycles. The cone-shaped STEPs consistently demonstrated a higher V_{oc}, thereby achieving superior voltage outputs across the applied pressure spectrum, with a 15% increase from 2.15 ± 0.03 mV $mmHg^{-1}$ in the cuboid-shaped sensor to 2.49 ± 0.02 mV $mmHg^{-1}$ in the cone-shaped sensor. Upon examining the mechanical and electrical responses of the STEPs, the conical structure has been substantiated as the better sensing morphology for pressure detection. This foundational understanding facilitates further exploration into the enhancement of sensor sensitivity through material optimization.

3.3. Material optimization of the STEPs

TENGs such as the STEPs fundamentally demonstrate inherent capacitive behaviour too as it is an electrostatic system, and the STEPs is also equivalent to a circuit consisting of a series of capacitors, as shown in Fig. 2d. In this figure, C_1 represents the capacitance between the bottom copper electrode and the reference electrode; C_2 represents the capacitance between the moving bottom electrode and the CB/PDMS structure; C_3 represents the electrical double layer (EDL) capacitance at the CB/PDMS structure and top copper electrode interface; C_4 represents the capacitance between the top copper electrode and the reference electrode. V_{oc} and transferred charge under short-circuit conditions (Q_{sc}) can be related by the following formula:[43,45]

$$Q_{SC} = V_{oc}C_0 \quad (3)$$

where C_0 represents the capacitance of the STEPs. When the bottom copper electrode is in contact with the CB/PDMS structure, V_{oc} and Q_{sc} are both 0. When the distance between the bottom copper electrode and CB/PDMS cone increases, V_{oc} and Q_{sc} can be derived with the following formula:[43,45]

$$V_{oc} = -\sigma A/2C_0 \quad (4)$$

$$Q_{SC} = -\sigma A/2 \quad (5)$$

where 'σ' represents the density of electrostatic charges generated at the surface of CB/PVP/PDMS structure and 'A' is the contact area between the bottom copper electrode and the CB/PDMS structure.

For materials optimization, we aim to increase σ by increasing the charge trapping ability of the material through doping of CB and PVP into PDMS. PDMS, a silicon-based organic polymer, is frequently employed in TENGs due to its flexibility, chemical stability, and biocompatibility, making it an ideal candidate for wearable and biomedical applications. However, the intrinsic limited conductivity of PDMS poses a challenge in fully realizing the output performance and sensitivity potential of TENGs. To address this, researchers have explored enhancing PDMS's performance by doping it with conductive fillers. These fillers, such as CB, graphene sheets, and carbon nanotubes, are introduced to increase the density of electrostatic charges (σ) generated on the surface of PDMS.[46–48] Consequently, the sensitivity of triboelectric pressure sensors is improved through an increased output voltage, which is supported by eqn (4).[49,50] Among the various fillers, CB is particularly advantageous due to its high conductivity, availability, cost-effectiveness, and low specific weight. The charge storage ability of CB-doped composites has been shown to effectively enhance the output performance of TENGs.[1] In our experimental framework, we investigated the effect of CB doping in PDMS on the sensitivity of the STEPs. We prepared the STEPs with varying CB content (0, 2, 4, 6, 8 wt%) and evaluated their performance. In Fig. 3a, the V_{oc} was observed to increase with the applied pressure, in the range of 0 to 70 mmHg. The introduction of CB into PDMS at a low weight percentage was found to improve the outputs of the STEPs. Notably, with only 2 wt% CB addition, a marked enhancement in performance was recorded from 1.33 ± 0.04 mV $mmHg^{-1}$ in pure PDMS to 2.49 ± 0.02 mV $mmHg^{-1}$, showing an overall 87% increase in sensitivity (***$p < 0.001$). This improvement is attributed to the additional charge trapping sites provided by CB particles within the PDMS matrix, which store the charges induced *via* the triboelectric effect, thus increasing the surface charge density and enhancing the STEPs' output.[1,51–54] Moreover, doping of CB into PDMS raises the dielectric constant of the composite, allowing for greater charge storage and optimizing the energy conversion efficiency. The V_{oc} output peaks at a CB content of 2 wt% across the applied pressure range. Beyond this concentration, a decline in sensing performance is observed, likely due to CB agglomeration, which leads to charge leakage and reduced V_{oc} outputs.[37,55] Conversely, PVP was also investigated for its potential to enhance TENG performance.

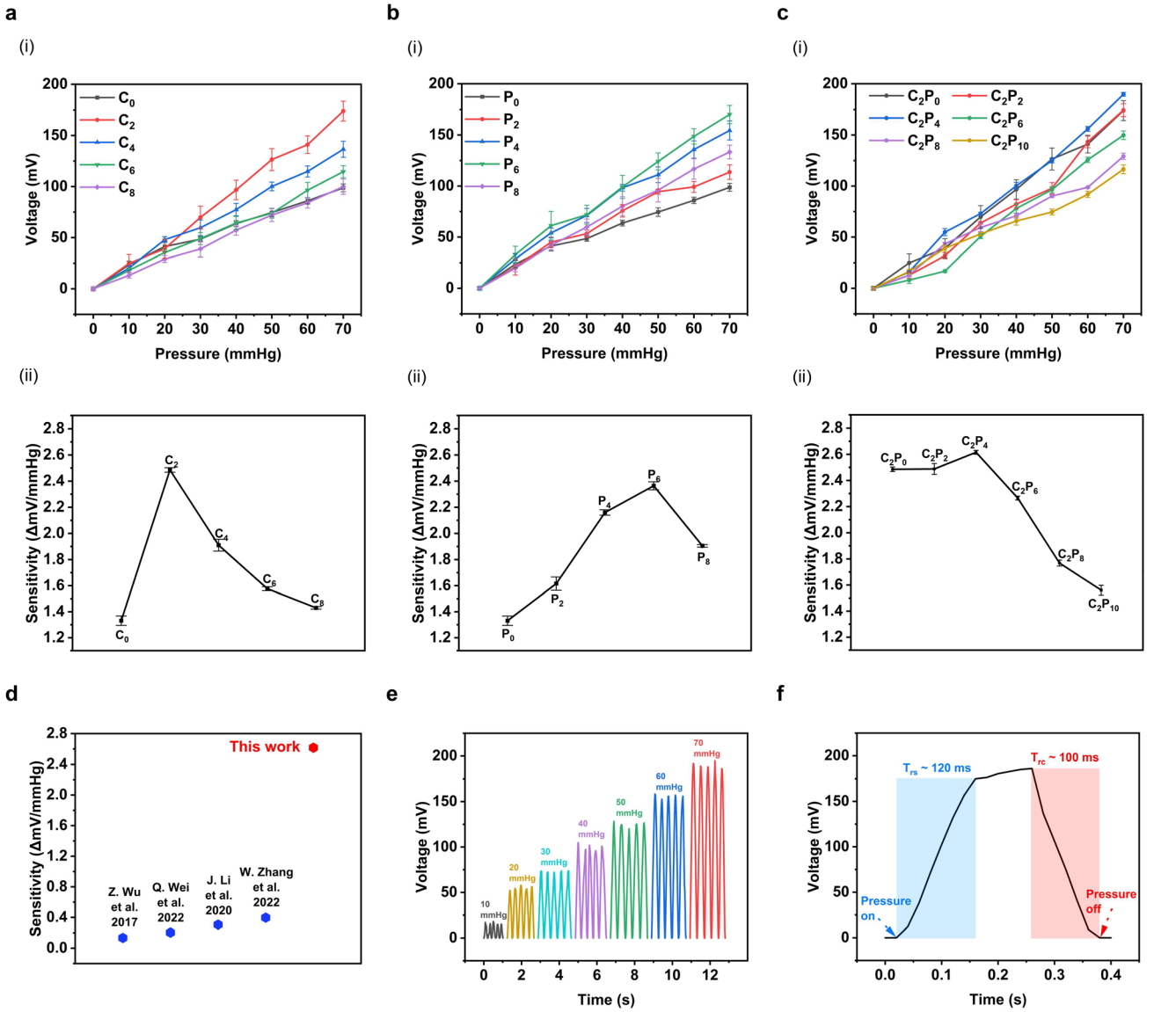

Fig. 3 Output characteristics of STEPs with varying dopant after performing background subtraction. (i) V_{oc} responses (n = 5) and (ii) sensitivity (n = 3) of STEPs under pressure ranging from 0 to 70 mmHg with (a) varying CB content for cone, (b) varying PVP content for cone and (c) varying CB/PVP contents for cone. Each data point is represented as mean ± SD. (d) Comparison of sensitivity obtained in this work with other reports.[1–4] (e) V_{oc} responses of C_2P_4 under different pressures in repeated cycles. (f) Response time and recovery time of STEPs.

PVP doping has been reported to increase the discharged energy density of a material, which in turn increases the dielectric constant of the material, and the dielectric properties of triboelectric materials increase the surface charge density (σ) as the surface charge is proportional to the relative permittivity of the triboelectric material.[49,50,52,54,56] PVP doping also leads to an increasing charge-trapping ability that increases the density of electrostatic charges (σ) generated on the surface of PDMS too, which thereby, will result in an elevated V_{oc} between the electrodes of the STEPs.[49,50,52,54,56] Considering these two benefits, PVP doping into PDMS was conducted, and STEPs with PVP contents of 0, 2, 4, 6, 8 wt% were synthesized and tested. Similar to CB, the V_{oc} increased with the pressure applied. In Fig. 3b, the optimal improvement was observed at a PVP content of 6 wt%, where the sensitivity increased by 78% from pure PDMS, to 2.36 ± 0.03 mV mmHg^{-1} (***$p < 0.001$). However, further increases in PVP content led to a diminishing return in performance, which could be ascribed to a saturation effect where the further addition of the dopant does not contribute to performance improvement and can even lead to negative effects due to issues like altered mechanical properties and increased viscosity.[57,58]

Following the identification of samples C_2 and P_6 as exhibiting the highest sensitivity, we extended our investigation to explore the synergistic effects of CB and PVP content on the performance of STEPs. Maintaining a constant CB concentration at 2 wt%, we varied the PVP content across 0, 2,

4, 6, 8, to 10 wt%. Fig. 3c revealed that the sample with 2 wt% CB and 4 wt% PVP, designated as C_2P_4, was the only composition that demonstrated an enhancement in sensitivity compared to the baseline sample C_2P_0 (***$p < 0.001$). The sensitivity increased by 96% compared to pure PDMS, to 2.61 ± 0.02 mV $mmHg^{-1}$. The observed decline in sensitivity beyond the C_2P_4 composition can be rationalized by the propensity for PVP and CB to form aggregates at higher concentrations, leading to the saturation effect.[1,59] Varying CB wt% with constant PVP content was not tested in dual doped systems due to two reasons. First, the sensitivity for P_6 (2.36 ± 0.03 mV $mmHg^{-1}$) is significantly lower than C_2 (2.49 ± 0.02 mV $mmHg^{-1}$) according to the two-sample *t*-test (**$p < 0.01$) (Fig. S3†). Second, comparing the sensitivity of C_0P_6 and C_2P_6, a significant drop sensitivity was observed from 2.36 ± 0.03 mV $mmHg^{-1}$ to 2.27 ± 0.02 mV $mmHg^{-1}$ (**$p < 0.01$) (Fig. S3†). Further increase in CB content for P_6 samples is expected to lead to a further drop in sensitivity. Through the strategic enhancement of the sensing material with the CB/PVP/PDMS composite, we achieved a notable augmentation in the sensor's performance for pressure ranging from 0 mmHg to 70 mmHg (detailed sensitivity for all STEPs tested is shown in Table S1†). This was evidenced by an elevated voltage output (sensitivity ≈ 2.61 ± 0.02 mV $mmHg^{-1}$), exemplary linearity ($R^2 \approx 0.996$) (Fig. S4†), and a swift response to applied pressure, showing substantial improvement compared to previous reports (Fig. 3d, Table S2†).[1–3,60,61] In the region after 70 mmHg, the STEPs reaches a saturation point, and a sharp drop in sensitivity can be seen in Fig. S5.†[62] This can be explained by the CB/PVP/PDMS cone starting to come into contact with the bottom copper electrode from the pressure of 70 mmHg onwards. This will lead to charges that were originally rendered at the two surfaces due to triboelectrification being neutralised, resulting in weaker repulsion between the like charges on the two copper electrodes, due to the lower positive charge of the bottom copper electrode. So, for per unit of pressure applied beyond 70 mmHg, the change in voltage will be lower, resulting in lowered sensitivity. The height for the PDMS supporting structure has been chosen such that the CB/PVP/PDMS cone will not touch the bottom copper electrode before 70 mmHg while the two copper electrodes are as close as possible to improve charge induction and sensitivity from 0 to 70 mmHg. This feature allows this TENG sensor design to be tailorable to different pressure ranges. Fig. 3e shows the V_{oc} responses of C_2P_4 under different pressures in repeated cycles. The response time (T_{rs}) and recovery time (T_{rc}) of STEPs are obtained through analysing the voltage response curve of a single cycle. As shown in Fig. 3f, T_{rs} has a value of 120 ms and T_{rc} has a value of 100 ms, which satisfy the requirements for dynamic tactile sensing.[63,64]

3.4. Potential application of the STEPs in human motion monitoring

Fig. 4a shows physical images and dimensions of the STEPs. In Fig. 4b and Video S2,† the sensor was positioned on the inner aspect of the elbow. Upon flexion of the arm, mechanical pressure was exerted on the STEPs, leading to an increase in V_{oc}. This voltage returned to its baseline value when the arm was relaxed. Fig. 4c and Video S3† illustrate the application of the STEPs in a grip-based scenario. The sensor was placed between the index finger and a cylindrical object. As the finger approached and exerted pressure on the beaker, there was a notable increase in V_{oc}, reflective of the higher pressure exerted on the object compared to the relaxed state of the finger. In Fig. 4d and Video S4,† the STEPs was placed at the inner surface of the index finger. During the demonstration, the finger was bent repeatedly, incrementally applying pressure on the STEPs across three consecutive trials. This was effectively captured by the sensor, as evidenced by a progressive increase in V_{oc} across the three tests. These experiments collectively demonstrate the STEPs' exceptional reliability and sensitivity in detecting and quantifying human motion.

3.5. Mechanism for multidirectional wireless pressure sensing

In our subsequent experiments, we focused on elucidating the impact of incrementing the number of STEPs from one to four, arranged in a series configuration. Empirical observations as presented in Fig. 5a indicate that the V_{oc} for the array of C_2P_4 reveals an appreciable increase of 20% to 3.14 ± 0.02 mV $mmHg^{-1}$, as evidenced by the steeper gradient in the voltage profile.

To facilitate wireless communication, we employed a Kivy-based application to construct a graphical user interface (GUI) coupled with a server following the Transmission Control Protocol (TCP). The circuit diagram is shown in Fig. 5b. For the quantification of V_{oc}, sensors are individually interfaced with the analog-to-digital converter (ADC) pins of a Maixduino board, set at a sampling rate of 250 Hz. Given the STEPs' sensitivity to extraneous factors, the initial 5000 measurement cycles are subjected to analysis and calibration adjustments. This stabilization process takes 20 seconds. Subsequent readings are averaged every 100 cycles and correlated with the pressure values. An ESP32 Wi-Fi module establishes a wireless network connection, which facilitates the dispatch of the processed data string, encapsulating the four pressure readings to the mobile server configured.

On the mobile server, the GUI architecture is configured to exhibit the connection status and the pressure readings from the sensors. Upon the establishment of a client–server connection, the server enters a persistent loop, continuously reading data, which corresponds to pressure readings from sensors, transmitted by the client. Due to Kivy's threading constraints, a method is invoked within the main thread to refresh the label widgets with the incoming data, thereby ensuring the real-time display of pressure readings from multiple directions, together with a change in colour, representing lower values with cold colours and higher values with warm colours as shown in Fig. 5c and Video S5.† The

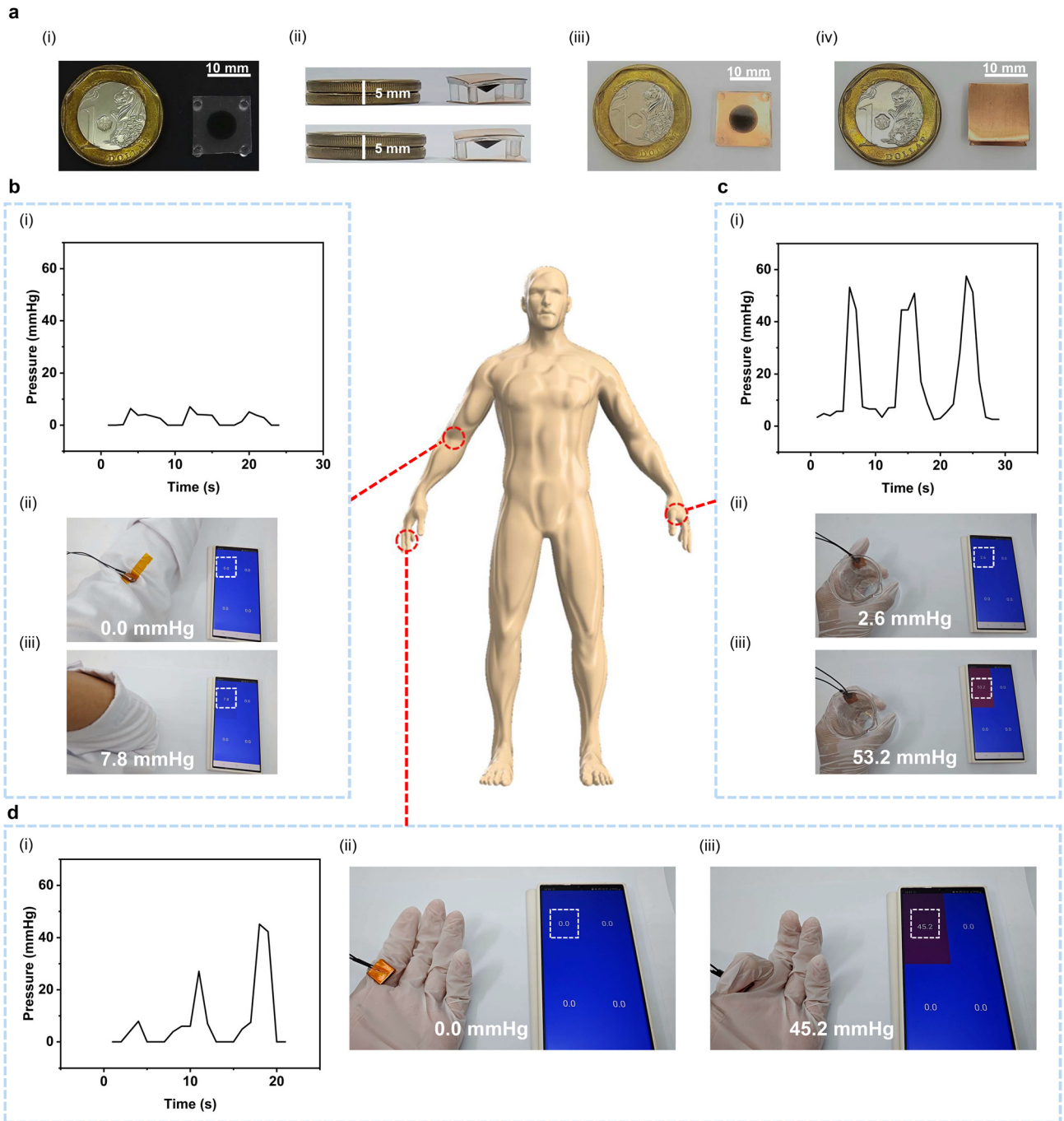

Fig. 4 Demonstration of the STEPs' potential in human motion detection. (a) Optical images of the STEPs. (i) Top view of CB/PVP/PDMS structure, (ii) side view of STEPs, (iii) bottom view of CB/PVP/PDMS structure with top copper electrode and (iv) top view of STEPs. (b and c) (i) V_{oc} responses, (ii) relaxed state and (iii) active state of STEPs during (b) arm flexion, (c) hand movements and (d) finger movements.

application was subsequently compiled into an executable file using Buildozer, enabling its deployment and operation on remote devices. Fig. 5d and e depict schematic representations of the STEPs, with the potential of functioning as an advanced human–machine interface. The system will be able to harnesses artificial intelligence to analyse and interpret signals captured by the sensor, thereby providing intelligent feedback. This will be a possible direction for future work.

Conclusion

In conclusion, leveraging a three-dimensional configuration that integrates both supporting and sensing structures, we have successfully developed STEPs, achieving high sensitivity, affordability, and real-time remote sensing capabilities, particularly in low-pressure scenarios. With the improvement of sensor materials and morphology, we have obtained the optimal weight percentages of 2 wt% CB and 4 wt% PVP

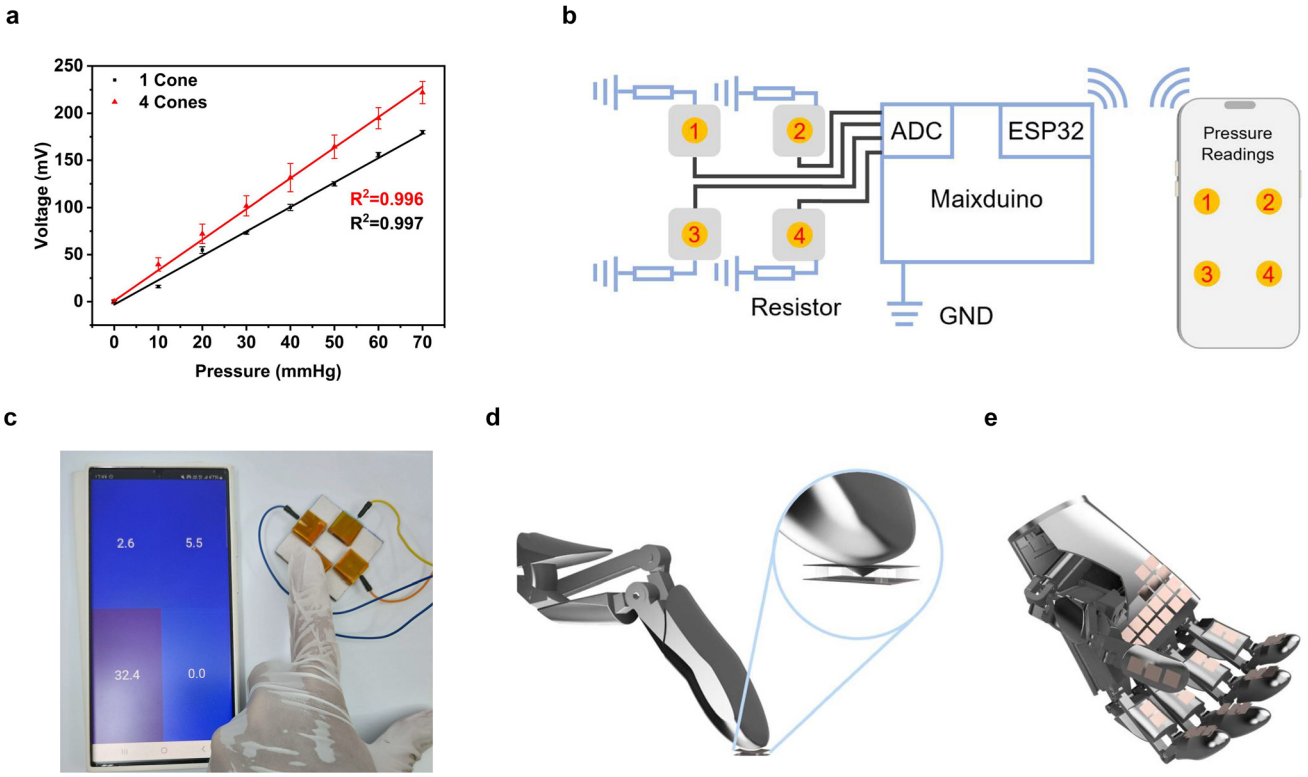

Fig. 5 Multidirectional sensing with the STEPs. (a) Mechano-electrical relationship with upscaling of number of cones (n = 5). (b and c) Smart indication system indicating the direction and magnitude of applied pressure by display on a remote device. (d) Schematic illustration showing the STEPs working as a human–machine interface. (e) Schematic illustration showing the STEPs' potential application for a humanoid robot.

doped into PDMS along with the cone-shaped structure, resulting in ultra-sensitivity with an excellent linearity ($R^2 \approx 0.996$) and a swift response to applied pressure ($T_{rs} \approx 120$ ms, $T_{rc} \approx 100$ ms) within the pressure range of 0 to 70 mmHg. The sensitivity of the optimal device is 2.61 ± 0.02 mV mmHg^{-1}, a 96% increase as compared to the pure PDMS cone-shaped sensor. By differentiating the location and magnitude of V_{oc}, the direction and degree of applied pressure could be realized and further utilized. The STEPs' enhanced sensitivity and self-powered, wireless nature marks a substantial leap in self-powered pressure sensing technology, showing great potential for high precision on-human monitoring, positioning itself as a considerable advancement over existing technologies. Its application in humanoid robotics promises more nuanced and safer human–robot interactions, while in virtual reality, it paves the way for more immersive and interactive experiences. Furthermore, the integration of this technology into the internet of things (IoT) ecosystem significantly enhances real-time data acquisition and processing, crucial for environmental monitoring and smart city applications.

Author contributions

JW and XTZ designed the sensors. JW fabricated and characterized the sensors. YZ printed the molds for sensors. JW, YZ and XTZ analysed data and discussed the results. JW wrote the draft. XTZ and YZ revised the manuscript.

Conflicts of interest

There are no conflicts to declare.

Acknowledgements

This research is supported by Agency for Science, Technology and Research (A*STAR) under A*STAR Career Development Fund C233312019 and Biomedical Engineering Programme C211318009.

Notes and references

1 W. Zhang, Y. Xi, E. Wang, X. Qu, Y. Yang, Y. Fan, B. Shi and Z. Li, *ACS Appl. Mater. Interfaces*, 2022, **14**, 20122–20131.
2 J. Li, Y. Long, F. Yang, H. Wei, Z. Zhang, Y. Wang, J. Wang, C. Li, C. Carlos, Y. Dong, Y. Wu, W. Cai and X. Wang, *Adv. Funct. Mater.*, 2020, **30**, 2002868.
3 Z. Wu and C. H. Ahn, presented in part at the 2017 19th International Conference on Solid-State Sensors, Actuators and Microsystems (TRANSDUCERS), 2017.
4 Q. Wei, G. Chen, H. Pan, Z. Ye, C. Au, C. Chen, X. Zhao, Y. Zhou, X. Xiao, H. Tai, Y. Jiang, G. Xie, Y. Su and J. Chen, *Small Methods*, 2022, **6**, 2101051.

5 A. Huseynov, *Journal of Social Research & Behavioral Sciences*, 2023, **23**, 9.
6 A. Leavy, L. Dick, M. Meletiou-Mavrotheris, E. Paparistodemou and E. Stylianou, *J. Comput. Assist. Learn.*, 2023, **39**, 1061–1082.
7 M. Parvini, A. H. Zarif, A. Nouruzi, N. Mokari, M. R. Javan, B. Abbasi, A. Ghasemi and H. Yanikomeroglu, *IEEE Open J. Commun. Soc.*, 2023, **4**, 464–517.
8 U. B. Saul, V. M. Reyes, G. Antonio Mattia, V. Raquel, L. M. Miguel Ángel and H. S. Marianella, *Mater. Des.*, 2023, **233**, 112273.
9 J. O. S. Silva, H. S. Granja, J. F. dos Santos, L. S. Freitas and E. M. Sussuchi, *J. Braz. Chem. Soc.*, 2023, **35**, 1–18.
10 S. Xuewei, L. Alamusi, Y. Bo, G. Lingxiao, N. Huiming, H. Kaiyan, L. Xiaolin, Z. Lidan, Z. Jiaofei, Y. Chao, G. Bin and H. Ning, *Carbon*, 2023, **216**, 118514.
11 A. Al Kuwaiti, K. Nazer, A. Al-Reedy, S. Al-Shehri, A. Al-Muhanna, A. V. Subbarayalu, D. Al Muhanna and F. A. Al-Muhanna, *J. Pers. Med.*, 2023, **13**, 951.
12 R. H. Baughman, A. A. Zakhidov and W. A. de Heer, *Science*, 2002, **297**, 787–792.
13 W. Eerenstein, N. D. Mathur and J. F. Scott, *Nature*, 2006, **442**, 759–765.
14 Z. L. Wang and J. Song, *Science*, 2006, **312**, 242–246.
15 W. Zhong Lin, *Faraday Discuss.*, 2014, **176**, 447–458.
16 Z. L. Wang, J. Chen and L. Lin, *Energy Environ. Sci.*, 2015, **8**, 2250–2282.
17 H. Yang, M. Deng, Q. Zeng, X. Zhang, J. Hu, Q. Tang, H. Yang, C. Hu, Y. Xi and Z. L. Wang, *ACS Nano*, 2020, **14**, 3328–3336.
18 T. Zhang, Z. Wen, Y. Liu, Z. Zhang, Y. Xie and X. Sun, *iScience*, 2020, **23**, 101813.
19 Z. Zhao, X. Pu, C. Du, L. Li, C. Jiang, W. Hu and Z. L. Wang, *ACS Nano*, 2016, **10**, 1780–1787.
20 U. Khan and S.-W. Kim, *ACS Nano*, 2016, **10**, 6429–6432.
21 X. Pu, W. Song, M. Liu, C. Sun, C. Du, C. Jiang, X. Huang, D. Zou, W. Hu and Z. L. Wang, *Adv. Energy Mater.*, 2016, **6**, 1601048.
22 Y. Yu, H. Sun, H. Orbay, F. Chen, C. G. England, W. Cai and X. Wang, *Nano Energy*, 2016, **27**, 275–281.
23 X. Pu, L. Li, M. Liu, C. Jiang, C. Du, Z. Zhao, W. Hu and Z. L. Wang, *Adv. Mater.*, 2016, **28**, 98–105.
24 J. Sun, H. Choi, S. Cha, D. Ahn, M. Choi, S. Park, Y. Cho, J. Lee, T.-E. Park and J.-J. Park, *Adv. Funct. Mater.*, 2022, **32**, 2109139.
25 T. Jing, B. Xu and Y. Yang, *Nano Energy*, 2020, **74**, 104856.
26 P.-Y. Feng, Z. Xia, B. Sun, X. Jing, H. Li, X. Tao, H.-Y. Mi and Y. Liu, *ACS Appl. Mater. Interfaces*, 2021, **13**, 16916–16927.
27 S. M. S. Rana, M. T. Rahman, S. Sharma, M. Salauddin, S. H. Yoon, C. Park, P. Maharjan, T. Bhatta and J. Y. Park, *Nano Energy*, 2021, **88**, 106300.
28 K. C. Pradel and N. Fukata, *Nano Energy*, 2021, **83**, 105856.
29 Y. Xie, J. Hu, H. Li, H.-Y. Mi, G. Ni, X. Zhu, X. Jing, Y. Wang, G. Zheng, C. Liu and C. Shen, *Nano Energy*, 2022, **93**, 106827.
30 P. Yin, K. C. Aw, X. Jiang, C. Xin, H. Guo, L. Tang, Y. Peng and Z. Li, *Nano Energy*, 2022, **95**, 106976.
31 H. Ouyang, Z. Li, M. Gu, Y. Hu, L. Xu, D. Jiang, S. Cheng, Y. Zou, Y. Deng, B. Shi, W. Hua, Y. Fan, Z. Li and Z. Wang, *Adv. Mater.*, 2021, **33**, 2102302.
32 H. Jiao, X. Lin, Y. Xiong, J. Han, Y. Liu, J. Yang, S. Wu, T. Jiang, Z. L. Wang and Q. Sun, *Nano Energy*, 2024, **120**, 109134.
33 T. Chen, Q. Shi, Z. Yang, J. Liu, H. Liu, L. Sun and C. Lee, *Nanomaterials*, 2018, **8**, 503.
34 X. Fu, H. Dong, Y. Zhen and W. Hu, *Small*, 2015, **11**, 3351–3356.
35 L. Lin, Y. Xie, S. Wang, W. Wu, S. Niu, X. Wen and Z. L. Wang, *ACS Nano*, 2013, **7**, 8266–8274.
36 K. Tao, Z. Chen, J. Yu, H. Zeng, J. Wu, Z. Wu, Q. Jia, P. Li, Y. Fu, H. Chang and W. Yuan, *Adv. Sci.*, 2022, **9**, 2104168.
37 Z. Wang, T. Bu, Y. Li, D. Wei, B. Tao, Z. Yin, C. Zhang and H. Wu, *ACS Appl. Mater. Interfaces*, 2021, **13**, 56320–56328.
38 X. Yaoxu, S. Youkang, T. Lan, H. Yougen, Z. Pengli, S. Rong and W. Ching-Ping, *Nano Energy*, 2020, **70**, 104436.
39 F. Zhang, Y. Zang, D. Huang, C.-A. Di and D. Zhu, *Nat. Commun.*, 2015, **6**, 8356.
40 J. F. Tilvawala Gopesh, *Soft Robot.*, 2021, **8**, 365–370.
41 H. Stefan and N. Patrizio, *Int. J. Solids Struct.*, 2003, **40**, 2767–2791.
42 R. S. Rivlin and D. W. Saunders, *Philos. Trans. R. Soc., A*, 1951, **243**, 251–288.
43 S. Niu and Z. L. Wang, *Nano Energy*, 2015, **14**, 161–192.
44 A. F. Diaz and R. M. Felix-Navarro, *J. Electrost.*, 2004, **62**, 277–290.
45 S. Niu, Y. Liu, S. Wang, L. Lin, Y. S. Zhou, Y. Hu and Z. L. Wang, *Adv. Funct. Mater.*, 2014, **24**, 3332–3340.
46 C. Ya-Wei, Z. Xiao-Nan, W. Gui-Gen, L. Gui-Zhong, Z. Da-Qiang, S. Na, L. Fei, Z. Hua-Yu, H. Jie-Cai and Y. Ya, *Nano Energy*, 2021, **81**, 105663.
47 U. Pierre Claver and G. Zhao, *Adv. Eng. Mater.*, 2021, **23**, 2001187.
48 F. F. Hatta, M. A. S. Mohammad Haniff and M. A. Mohamed, *Int. J. Energy Res.*, 2022, **46**, 544–576.
49 S. Cai, C. Han, X. Cao, Q. Sun, X. Liu, Y. Wang, P. Zhao and Z. Wu, *Appl. Phys. Lett.*, 2023, **123**, 183903.
50 M. P. Kim, D.-S. Um, Y.-E. Shin and H. Ko, *Nanoscale Res. Lett.*, 2021, **16**, 35.
51 J. H. Choi, Y. Ra, S. Cho, M. La, S. J. Park and D. Choi, *Compos. Sci. Technol.*, 2021, **207**, 108680.
52 Y. Liu, J. Mo, Q. Fu, Y. Lu, N. Zhang, S. Wang and S. Nie, *Adv. Funct. Mater.*, 2020, **30**, 2004714.
53 P. K. Szewczyk, A. E. Taşlı, J. Knapczyk-Korczak and U. Stachewicz, *Compos. Sci. Technol.*, 2023, **243**, 110247.
54 Z. Abbas, M. Anithkumar, A. P. S. Prasanna, N. Hussain, S.-J. Kim and S. M. Mobin, *J. Mater. Chem. A*, 2023, **11**, 26531–26542.
55 H. Ding, W. Zang, J. Li, Y. Jiang, H. Zou, N. Ning, M. Tian and L. Zhang, *Compos. Commun.*, 2022, **31**, 101132.
56 K. Woo Kyum, W. Chaoxing and K. Tae Whan, *Appl. Surf. Sci.*, 2018, **444**, 65–70.

57 A. D. Buckingham and J. A. Pople, *Optical, Electric and Magnetic Properties of Molecules*, ed. D. C. Clary and B. J. Orr, Elsevier Science B.V., Amsterdam, 1997, pp. 49–53.
58 Z. Adamczyk, in *Interface Science and Technology*, ed. Z. Adamczyk, Elsevier, 2006, vol. 9, pp. 15–196.
59 S. Zhao, J. Li, D. Cao, G. Zhang, J. Li, K. Li, Y. Yang, W. Wang, Y. Jin, R. Sun and C.-P. Wong, *ACS Appl. Mater. Interfaces*, 2017, **9**, 12147–12164.
60 T. Li, J. Zou, F. Xing, M. Zhang, X. Cao, N. Wang and Z. L. Wang, *ACS Nano*, 2017, **11**, 3950–3956.
61 Z. Liu, Y. Ma, H. Ouyang, B. Shi, N. Li, D. Jiang, F. Xie, D. Qu, Y. Zou, Y. Huang, H. Li, C. Zhao, P. Tan, M. Yu, Y. Fan, H. Zhang, Z. L. Wang and Z. Li, *Adv. Funct. Mater.*, 2019, **29**, 1807560.
62 C. Garcia, I. Trendafilova, R. Guzman de Villoria and J. Sanchez del Rio, *Nano Energy*, 2018, **50**, 401–409.
63 Y. Liu, R. Bao, J. Tao, J. Li, M. Dong and C. Pan, *Sci. Bull.*, 2020, **65**, 70–88.
64 T. Zhang, Z. Wen, H. Lei, Z. Gao, Y. Chen, Y. Zhang, J. Liu, Y. Xie and X. Sun, *Nano Energy*, 2021, **87**, 106215.